Symmetry-driven valleytronics in the single-layer tin chalcogenides SnS and SnSe

Nguyen Thanh Tien [1,*] Pham Thi Bich Thao [1] Nguyen Thi Han [2] and Vo Khuong Dien [3,4,†]

[1]*College of Natural Sciences, Can Tho University, 3-2 Road, Can Tho City 94000, Vietnam*
[2]*Faculty of Materials Science and Engineering, Phenikaa University, Yen Nghia, Ha Dong, Hanoi 12116, Vietnam*
[3]*Division of Applied Physics, Dong Nai Technology University, Bien Hoa City, Vietnam*
[4]*Faculty of Engineering, Dong Nai Technology University, Bien Hoa City, Vietnam*

The concept of valleytronics has recently gained considerable research attention due to its intriguing physical phenomena and practical applications in optoelectronics and quantum information. In this study, by employing the Green function-Bethe-Salpeter equation (GW-BSE) calculations and symmetry analysis, we demonstrate that single-layer orthorhombic SnS and SnSe possess remarkable carrier mobility and exceptional excitonic effects. These materials display spontaneous linearly polarized optical selectivity, a behavior that differs from the valley-selective circular dichroism observed in the hexagonal lattices. Specifically, when the two-dimensional tin chalcogenide is subjected to a zigzag polarization of light, only the A exciton becomes optically active, while the B exciton remains dark. The armchair-polarized light triggers the opposite behavior. This selective optical excitation arises from the symmetry of the bands under mirror symmetry. Additionally, the study reveals a strong coupling between valley physics and ferroelectricity in layered tin chalcogenides, enabling the manipulation of exciton polarization. Layered tin chalcogenides thus emerge as promising candidates for valleytronic materials.

I. INTRODUCTION

Since the inception of monolayer graphene [1], two-dimensional (2D) materials have become a focal point of extensive research owing to their exceptional properties and potential applications [2]. Their unique attributes fuel investigations across various nanoscience realms, particularly optoelectronics, quantum information, and energy harvesting [3,4]. Valleytronics [5,6], a burgeoning area of exploration, holds promise for various applications. Exploring odd layers [7] or specific experimental setups such as strong electronic or magnetic fields [8] and cryogenic temperatures [9] reveal the potential for valleytronics detection. For example, monolayer MoS_2 and WSe_2 exhibit two energetically degenerate valleys in K and K' in the Brillouin zone [10,11]. These valleys could be coupled with right and left circularly polarized light, respectively [12,13], and hold significance for quantum information and optoelectronic pursuits. However, the stringent demands present substantial practical hurdles, posing a significant obstacle in leveraging this technology for real-world applications.

While circular dichroism has dominated investigations of valley excitons in transition metal dichalcogenides (TMDs), the exploration of valleys triggered by linear dichroism has recently emerged in black phosphorus [14,15] due to its lower lattice symmetry. However, such material offers just a single-fold linear dichroism property, limiting its capacity to probe valley-related characteristics. Layered SnS and SnSe are sizable gap semiconductors that are widely uti-

lized for thermoelectrics [16], photocatalysis [17], and sensors [18–20]. The presence of notable spontaneous in-plane polarization also makes tin chalcogenide particularly attractive for ferroelectric applications [21,22]. Furthermore, layered SnS and SnSe hold promise: Theorists predicted the selective excitation of paired valleys along the armchair and zigzag directions using differently polarized linear light [23]. Take thin-film SnS for example, with its puckered-layered structure, displaying marked anisotropy between the armchair (y) and zigzag (x) directions. This anisotropy manifests in directional behavior in in-plane electronic mobility [24], Raman response [25], and photoluminescence spectra [26]. Despite that, the mechanism for spontaneous valley selective excitation in layered SnS is unclear, as the treating accuracy of fully many-body first-principles calculations essential for understanding such processes surpasses the capability of existing theoretical methods [23]. The fundamental questions arise regarding the underlying physical mechanisms governing these processes of valley selectivity and how valley physics might interact with excitonic effects and ferroelectricity.

In this work, we explore SnS and SnSe monolayers, characterized by strong in-plane electrical and optical anisotropy. We observed two distinct exciton peaks in their absorbance spectra, suggesting potential applications in optoelectronic and quantum information. Utilizing *ab initio Green function-Bethe-Salpeter equation* (GW-BSE) calculations and symmetry analysis, we demonstrate that the constituent holes and electrons arise from nearly degenerate yet distinct valleys along the $\Gamma - X$ and $\Gamma - Y$ directions, respectively. In contrast to TMDs, where exciton valleys couple with circularly polarized photons [27], the valley excitons in SnS and SnSe interact with photons of opposite linear polarization. Specifically, the exciton located in the X valley strongly interacts

*nttien@ctu.edu.vn
†Corresponding author: vokhuongdien@dntu.edu.vn
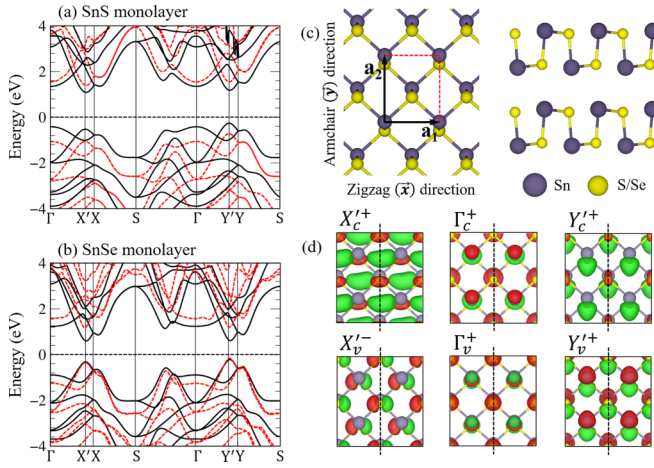
FIG. 1. Electronic properties of SnS and SnSe monolayers: Electronic band structure of (a) SnS and (b) SnSe monolayers. The black line indicates the band dispersion under the DFT level of theory, while the red-dashed one shows the band structure of studied materials under G0W0 correction. The G0W0 quasiparticle band structure in this work was achieved under WANNIER90 codes [28]. (c) Top view of the single-layer SnS and side view of its bulk counterpart. The red square indicates the computed unit cell. (d) Electronic wave functions of single-layer SnS at the critical points. The green and red isosurfaces indicate the positive and negative phases of the wave function, respectively. The black-dashed lines denote the M_z mirror plane and $(+)$ and $(-)$ signs above each panel indicate the even and odd parity, respectively.

with zigzag-polarized light, whereas the exciton resized in the Y valley exhibits a similar behavior with light polarized along the armchair direction. Moreover, in layered SnS and SnSe, the distortion of tin and chalcogenide atoms may lead to strong ferroelectric order along the in-plane direction. Such ferroelectricity is strongly coupled with valley physics. The polarization of exciton valleys could be switched or even turned off according to the distortion of the lattice crystal. SnS and SnSe monolayers emerge as promising materials for applications in valleytronics, thereby opening new avenues for technological advancement.

II. RESULTS AND DISCUSSIONS

We first look at the stable geometric structure of single-layer SnS and SnSe [Fig. 1(c)]. The bulk form of such materials processes the orthorhombic crystal (Pnma) similar to that of black phosphorus [29,30]. In which, the interlayers are weakly held together through a weak van-der-Waal interaction, making the exfoliation of atomically thin film or even monolayer could be assessable [31]. In the case of single-layer SnS, the lattice constants along the zigzag and armchair directions were 4.08 Å and 4.28 Å, respectively. Similarly, for the SnSe monolayer, these values were measured at 4.30 and 4.36 Å. Our calculated results align well with prior theoretical predictions [32,33] and experimental observations [31]. Due to the relative displacement between the tin and chalcogenide atoms, the mirror symmetry along the armchair direction (M_a) and the centrosymmetric is broken, while the mirror plane along the zigzag one (M_z) is well preserved, indicating

the in-plane ferroelectric phase [21,34,35]. The orthorhombic symmetry of the tin chalcogenide monolayers leads to distinctive physical properties, including significantly larger piezoelectricity compared to other 2D materials [33], intrinsic in-plane ferroelectricity [34,36], and unique Berry curvature (BC) dipole [37]. This study further confirms that this unique symmetry is responsible for valley-selective linear dichroism.

Figures 1(a) and 1(b) display the electronic band structures at high-symmetry points, calculated through Kohn-Sham density-functional theory (DFT), as well as G0W0 quasiparticle techniques. SnS and SnSe monolayers display indirect band gaps of 1.34 and 0.81 eV, respectively. When the G0W0 correction is applied, the band gap values for these systems increase to 2.19 and 1.40 eV, respectively. These theoretical findings align consistently with current predictions [30,38,39]. Analogously to phosphorene [29] and GeS [40], the single layer of SnS and SnSe manifests anisotropic electronic behaviors, where the effective carrier mass along the $\Gamma - Y$ direction is smaller than that along the $\Gamma - X$ direction. The relatively small effective mass indicated that these materials possess high carrier transport properties. The calculated carrier mobility of monolayer SnS for the hole at valence band minima (VBM) and electron at conduction band maxima (CBM) along the armchair directions, respectively, is 0.61×10^3 cm^{-2}V^{-1}s^{-1} and 2.32×10^3 cm^{-2}.V^{-1}.s^{-1}. The mobility of the hole and electron for single-layer SnSe is 1.34×10^3 cm^{-2}.V^{-1}.s^{-1} and 38.16×10^3 cm^{-2}.V^{-1}.s^{-1}. These values are much higher than those of 2D TMDs [41] and comparable with those of black phosphorus [42].

There are two distinct valleys at X' and Y' in reciprocal space, which are not located at the high-symmetry points but lightly shift along $\Gamma - X$, and $\Gamma - Y$ directions, Fig. 7(b). Due to the broken inversion symmetry, the degeneracy of these valleys has been lifted. In particular, the direct valence-to-conduction of SnS at X' and Y' in the quasiparticle GW band is 2.63 and 2.35 eV, respectively. The corresponding values for single-layer SnSe are 1.51 and 1.36 eV. The spontaneous valley splitting is a key feature of the linear dichroism properties. The valley polarization in orthorhombic tin chalcogenide is comparable to that induced by external perturbations absorbed in hexagonal crystals. For instance, under a high magnetic field (B = 8.4 T), WSe$_2$ can induce a valley splitting of 200 meV [43], while MoTe$_2$ on the EuO substrate can exhibit a valley splitting of 300 meV [44]. The introduction of spin-orbit coupling (SOC) reduces the band gap of 2D tin sulfide by 68 meV [Fig. 7(c)], and for single-layer tin selenide, the corresponding reduction is 42 meV [Fig. 7(d)]. While the overall energy dispersion in the vicinity of the valleys does not change significantly [30].

The real [Fig. 1(d)] and the reciprocal space [Figs. 7(e)–7(h)] electronic wave functions of SnS and SnSe monolayers indicated that their VBM is dominated by the S/Se atom, while the Sn atom mostly distributes at the higher energy regime in CBM. In detail, the VBM and CBM of SnS/SnSe at the Γ are almost occupied by the p_z orbital of S/Se and Sn atoms, respectively. While for the X' (Y') valley, VBM and CBM, correspondingly, are dominated by p_x (p_y) orbitals of chalcogenide and tin atoms. In addition to the orbital characteristics of the specific valleys, the symmetry of the electronic wave function is an important feature for compre-

TABLE I. Parity of the electronic states in single-layer SnS under in-plane mirror symmetry at different points of the Brillouin zone, and the electronic transition dipole from the first valence band (v) to the first conduction band (c) for the polarization along the zigzag direction $|\langle\varphi_v|\mathbf{p}_z|\varphi_c\rangle|$, and armchair direction $|\langle\varphi_v|\mathbf{p}_a|\varphi_c\rangle|$. 1 denotes optically allowed, while 0 means the transition is forbidden.

Valley	φ_v	φ_c	$|\langle\varphi_v|\mathbf{p}_z|\varphi_c\rangle|$	$|\langle\varphi_v|\mathbf{p}_a|\varphi_c\rangle|$
Γ	+	+	0	1
X'	−	+	1	0
Y'	+	+	0	1

hending optical anisotropy. In the context of the SnS and SnSe monolayers, their crystal structure manifests mirror symmetry only in the zigzag direction (M_z), as shown in Fig. 1(d). This specific symmetry classification enables to categorization of wave function parity as either even (+) or odd (−) eigenstates of M_z. Here, the even function displays symmetric properties about the mirror plane, while the odd electronic states showcase antisymmetric features through this plane. The parity of the bands at specific critical points is manifested in Fig. 1(d) and listed in Table I. The electronic functions in the occupied and unoccupied states at the Γ and Y' valleys display identical even (+) parity, whereas the X' valley exhibits the opposite behavior.

To explore optical responses and excitonic effects, we solved the BSE on top of G0W0 calculations [45]:

$$(E_{c\mathbf{k}} - E_{v\mathbf{k}})E_{cv\mathbf{k}}^S + \sum_{c'v'\mathbf{k'}} A_{c'v'\mathbf{k'}}^S \langle cv\mathbf{k}|K_{eh}|v'c'\mathbf{k'}\rangle = A_{cv\mathbf{k}}^S \Omega^S,$$
(1)

in which, $A_{cv\mathbf{k}}^S$ is the k-space exciton envelope wave function, Ω^S is the corresponding eigenvalue, and K_{eh} is the electron-hole interaction kernel. The details of the convergence properties of the BSE are shown in Fig. 6. The real-space exciton wave function $\phi_S(r_h, r_e)$ could be further given by

$$\phi_S(\mathbf{r}_h, \mathbf{r}_e) = \sum_{cv\mathbf{k}} A_{cv\mathbf{k}}^S \varphi_{c\mathbf{k}}(\mathbf{r}_e)\varphi_{v\mathbf{k}}^*(\mathbf{r}_h),$$
(2)

where $\varphi_{c\mathbf{k}}(\mathbf{r}_e)$ represents the electron wave function, and $\varphi_{v\mathbf{k}}^*(\mathbf{r}_h)$ corresponds to the hole wave function.

The GW-BSE approach, as depicted in Eq. (1), enables the direct computation of the electron-hole eigenstate within the correlated two-particle wave function. However, it does not account for the interaction between the quasiparticle and electromagnetic fields. The formula for the oscillator strength, denoting the connection between an external field and the exciton state, is expressed as follows:

$$\sigma^S(\mathbf{e}) = \frac{\left|\sum_{cv\mathbf{k}} A_{cv\mathbf{k}}^S p_{cv\mathbf{k}}^{\mathbf{e}}\right|^2}{\Omega^S},$$
(3)

where, the exciton wave function $A_{cv\mathbf{k}}^S$ and its eigenvalue Ω^S are achieved through solving BSE in Eq. (1), and the interband transition matrix element $p_{cv\mathbf{k}}^{\mathbf{e}}$ is purely related to the single-particle excitation picture [Eq. (B1)].

The absorption spectra of the SnS and SnSe monolayers resulting from linearly polarized light are presented in Figs. 2(a)
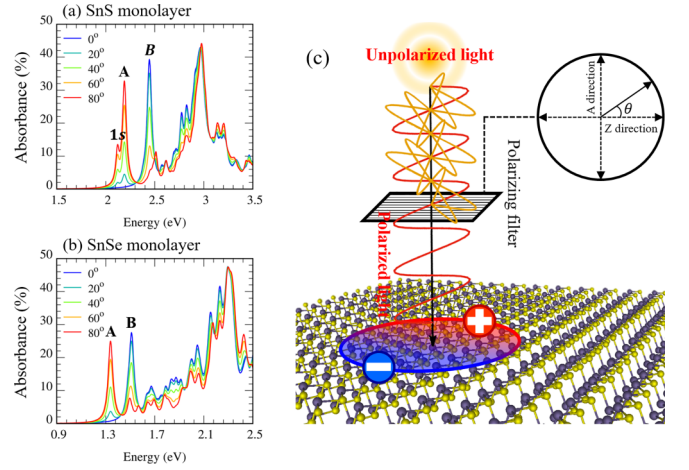
FIG. 2. The absorption spectrum of monolayer (a) SnS and (b) SnSe as a function of polarization of light. The spectra are achieved with a Lorentzian width of 20 meV. (c) The polarization of incident light could be effectively controlled via the polarizing filter. By manipulating the orientation of incident light, we can arbitrarily modulate the exciton of which valley can be optically excited.

and 2(b). For computational efficiency, our discussions here solely focus on the optical properties, excluding SOC effects. The absorption spectra exhibit three (two) prominent peaks, labeled as 1s, A, and B (A and B), with excitation energies of 2.12, 2.20, and 3.38 eV (1.34 and 1.47 eV), respectively. The former(s) originate solely from the Γ and/or Y' valley, while the latter is associated with the X' valley [Figs. 3(a) and 3(b). These distinct physical mechanisms that arise in the reciprocal space are intricately reflected in the angle-dependent optical absorption spectra observed in experimental measurements. For instance, when the light polarization aligns along the armchair direction of monolayer SnS, the 1s, and A excitons exhibit the highest intensity, while the B exciton is nearly absent. Conversely, at smaller polarization angles, the B exciton becomes evident, while the 1s and A excitons become inactive. Due to quantum confinement and the absence of vertical dielectric screening, the exciton binding energy (E_{xb}), determined by the difference between the fundamental band gap (E_g) and the first exciton energy (E_S), is predicted to be robust in these studied materials. Specifically, the E_{xb} of SnS and SnSe monolayers is 0.52 and 0.14 eV, respectively, falling within the range observed in well-studied excitonic materials [46,47].

Figure 3 illustrates the squared amplitudes of the exciton wave functions in reciprocal space alongside the energy diagram of the exciton states within the SnS monolayer. Due to the unique screening characteristics of low-dimensional materials, e.g., Keldysh-like dielectric function [48], higher-order excited excitonic states with larger e-h spatial separation will experience a smaller portion of screening from the surroundings, and thus leads to enhanced Coulomb attraction. As a consequence, the excitonic energy diagram diverges from the typical Rydberg series observed in the 2D hydrogenic model [49]. For example, the activation energy of 2s excitons is larger than that of $2p_x$ and $2p_y$ excitons. Moreover, the 1s exciton state, which originates from transitions between the first valence and conduction bands at the center Γ, emerges as
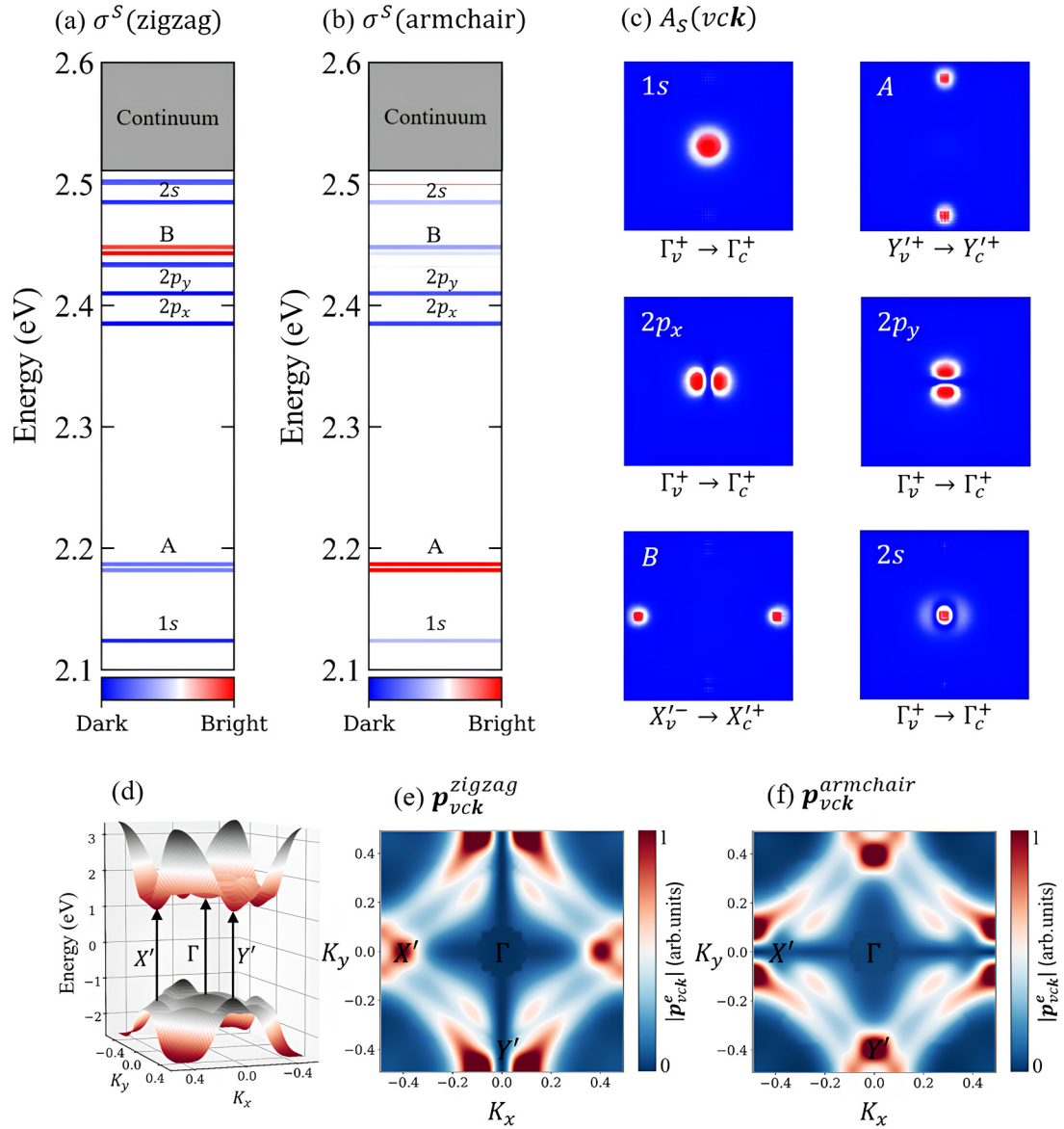
FIG. 3. The excitonic properties of single-layer SnS: Exciton energy spectrum of the SnS monolayer for the polarization of light along the (a) zigzag and (b) armchair directions. Excitonic amplitudes (color scale in the bottom panels) are normalized with respect to the brightest exciton among all of the exciton states from blue (dark exciton) to red (bright exciton). (c) the k-space distribution of the envelope functions for the first six bought excitons. The exciton states are labeled with primary and azimuthal quantum numbers according to their nodal structure in the radial and azimuthal directions, respectively. The valence-to-conduction band transition is indicated below each exciton wave function. (d) 3D electronic energy spectra of single-layer SnS with two emerging valleys X' and Y' in the frequency of interest. The modulus of the optical transition dipole moment ($|\mathbf{p}^e_{vck}|$) for the polarization of light along (e) zigzag and (f) armchair directions. For the polarization of light along the zigzag direction, $|\mathbf{p}^e_{vck}|$ gets a significant value at the X' valley, while it almost vanished at the Γ and Y' valleys. The opposite behavior is true for the polarization of light along the armchair direction.

the lowest state despite its origin from a valley with higher energy. This is mainly due to the relatively large effective mass of both the electron and the hole at the Γ point. Additionally, there exist two distinct exciton states labeled A and B, which are precisely situated at the X' and Y' valleys. These states play a pivotal role in the low-frequency optical response as discussed earlier. Figure 3 also shows the exciton dipole, which is represented by the oscillation strength σ^S (e) in Eq. (3). In addition to the bright excitons that are displayed on the adsorption spectra, there are a lot of dark states with

insignificant oscillation strength. The darkness and brightness of the exciton state are also very sensitive to the orientation of the incident photon. Quantitatively, we calculate the polarization coefficient $\eta = \frac{\sigma^S(zig) - \sigma^S(arm)}{\sigma^S(zig) + \sigma^S(arm)} \times 100\%$, where $\sigma^S(zig)$ and $\sigma^S(arm)$ denote the oscillation strength of the S exciton excited by linearly polarized zigzag and armchair light. In the SnS monolayer, η exceeds 83% and 62% for the excitons A and B, while the corresponding values for single-layer SnSe are 91% and 76%.

Since the interaction between the excited hole and the excited electron is an attractive coupling and is an even function. The selective polarization is now mainly related to the single-particle excitation picture addressed by the modulus of transition dipole moment between the initial $|\varphi_v\rangle$ and the final electronic states $|\varphi_c\rangle$: $|\langle\varphi_v|\mathbf{p_n}|\varphi_c\rangle|^2$. Here, p_n (where $n = a, z$) is the momentum operator that represents the direction of the polarization of the photon. Optical transitions occur only when the $|\langle\varphi_v|\mathbf{p_n}|\varphi_c\rangle|^2$ matrix elements do not disappear. The origin of linear dichroism could be understood by symmetry analysis [50]. The crystal symmetry dictates that the single-particle transition dipole ($\mathbf{p_n}$) undergoes a sign reversal ($\mathbf{p}_z$ to $-\mathbf{p}_z$) when illuminated by light polarized along the zigzag direction, while it remains constant ($\mathbf{p}_a$ to $\mathbf{p}_a$) under armchair polarization. This behavior suggests that single-particle optical transitions along the zigzag (or armchair) direction selectively occur between electron states characterized by opposite (or identical) parities following the M_z symmetry. Figures 3(e) and 3(f) illustrates the k-dependent transition dipole moment. There are large electronic dipoles localized at the X' and Y' valleys, but they exhibit the opposite behavior. Specifically, when incident light aligns with the armchair direction, optical activity occurs in transitions from the valence to the conduction bands at Γ and Y'. This arises due to both bands displaying an even (+) parity [Fig. 1(d)]. Conversely, with zigzag-polarized light, there are no contrasting parities between these bands, resulting in a zero-transition dipole moment. In contrast, when the light aligns along the zigzag direction, a significant dipole emerges at the X' valley, while the dipole at the Γ and Y' valleys almost diminishes. The symmetry-driven optical selectivity was also detected in monolayer GaSe and GaTe [50]. However, because of symmetry differences, their exciton states couple with electromagnetic waves in different manners. For example, these materials exhibit sharp exciton peaks, the presence of which in the absorbance strongly depends on the angle of incident light relative to the normal direction of the plane.

Apart from the exciton wave function in k space, the electron-hole correlation functions in real space, denoted as $|\phi_S(\mathbf{r}_h, \mathbf{r}_e)|^2$, offer valuable insights into specific exciton symmetries and their localization. To investigate exciton symmetry, we positioned the hole near the Sn atom and plotted the electron density as a function of $\mathbf{r}_e$ onto the x-y plane. Figure 4 illustrates that while the wave functions of the A and B excitons are confined within the monolayer's limits, they exhibit an extended characteristic along the in-plane direction. These envelope functions span multiple unit cells of the tin chalcogenide monolayer, a characteristic behavior akin to Wannier-Mott excitons [52]. Analyzing their wave functions allows us to deduce selection rules in this context. Although the wave function expresses the circle characteristics, the electron component of the A exciton mostly aligns along the armchair direction, showcasing the $Sn - 5p_y$ characteristic of the Y' valley. Conversely, the B exciton localizes along the zigzag direction, reflecting the $Sn - 5p_x$ feature of the X' valley. The excited exciton states of the SnSe monolayer are plotted in Figs. 4(c) and 4(d). These states are much less localized than that of single-layer SnS followed by smaller binding energies. These states also obey the same selection rules as those depicted in the SnS counterpart.
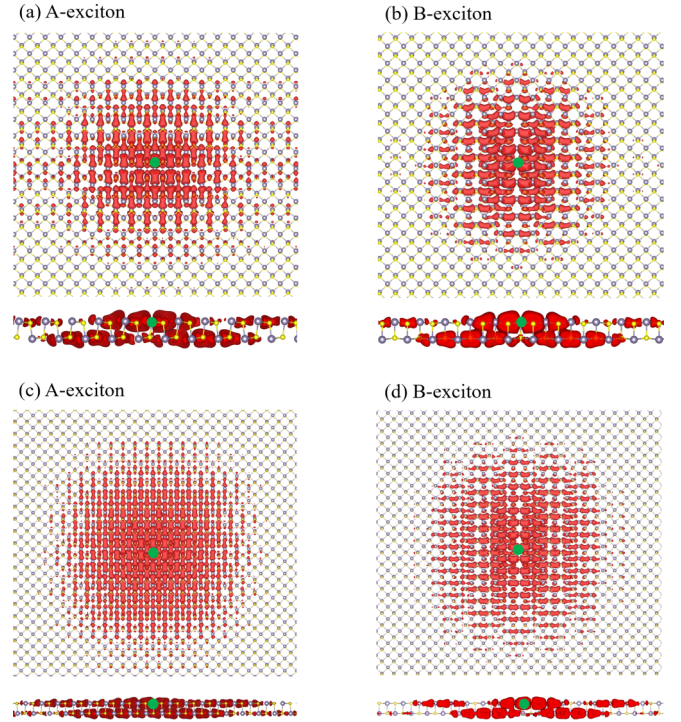
FIG. 4. Top and side views of the spatial Exciton amplitudes for (a) A-exciton and (b) B-exciton in monolayer SnS. (c) and (d) depict analogous plots for single-layer SnSe. The green sphere denotes the position of the hole. The visualization of the real-space exciton wave functions was generated using the exciting code [51], employing identical criteria as in VASP, but restricted to $15 \times 15 \times 1$ KPOINTS.

Berry curvature (BC) is another essential physical property in the context of valleytronics. The Kudo formula [53] provides an expression for BC:

$$\Omega_{n\mathbf{k}} = \sum_n \sum_{n \neq n'} f_n \frac{\langle\varphi_{n\mathbf{k}}|v_x|\varphi_{n'\mathbf{k}}\rangle\langle\varphi_{n'\mathbf{k}}|v_y|\varphi_{n\mathbf{k}}\rangle}{(E_{n\mathbf{k}} - E_{n'\mathbf{k}})^2}. \quad (4)$$

Here, f_n represents the Fermi-Dirac distribution function, $\varphi_{n(n')\mathbf{k}}$ stands for the Bloch wave function with eigenvalue $E_{n(n')\mathbf{k}}$, and $v_x(v_y)$ denotes the velocity operator along the $x(y)$ direction. The BC of the orthorhombic SnS monolayer across the 2D Brillouin zone are illustrated in Fig. 5(a). Unlike the hexagonal crystal, such as β-SnS, which exhibits contrasting BC distributed around K and K' of the hexagonal Brillouin zone, the broken inversion symmetry of orthorhombic tin chalcogenide systems results in a distinct polarization-dependent distribution of BC. Considering the M_z mirror symmetry, the BC of the 2D SnS follows the property: $\Omega_n(k_x, k_y) = -\Omega_n(-k_x, k_y)$. Consequently, this leads to the emergence of positive and negative BC features, which are inherently linked to the BC dipole discussed in previous works [37,55]. Furthermore, the direction of BC polarization reverses with the reversal of structural distortion. The BC dipole is predicted to be directly coupled with ferroelectricity, as elaborated hereafter.

In principle, the presence of mirror symmetry and the confinement of the electron wave function in the 2D Brillouin zone are responsible for the valley polarization selection roles. The electron-hole correlation pairs excited via
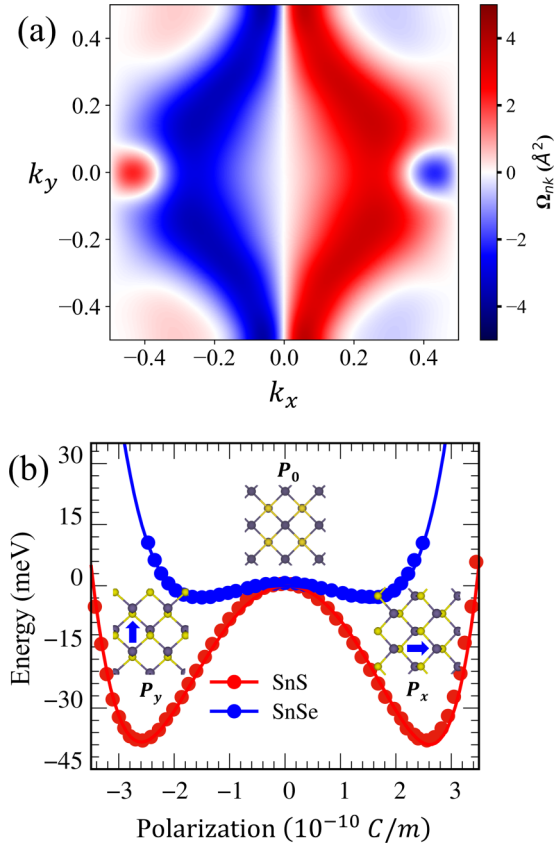
FIG. 5. (a) The calculated out-of-plane Berry curvature (BC) of SnS monolayer mapped in the 2D Brillouin zone. The BC was computed using WANNIER90 codes [28], with the Fermi energy set at the midpoint of the band gap. (b) Double-well potential as a function of the polarization in monolayers SnS and SnSe. Two ferroelectric phases with spontaneous polarization along the x and y directions and the paraelectric configuration, respectively, are denoted as P_x, P_y, and P_0. The circles indicate the calculated values achieved from the Modern Theory of Polarization [54], while the solid lines present the fitting function using Landau-Ginzburg expansion [34].

linear dichroism of light could act as the exciton qubits, offering a facilitated way to manipulate and store information. The similar spontaneous valley polarization caused by crystalline symmetry breaking was also found in tetragonal LaOMX_2 monolayers [56]. Interestingly, different from the traditional valleytronic materials and LaOMX_2, the monolayer of SnS and SnSe can exhibit a more interesting phenomenon. As shown in Fig. 5(b), the tin and chalcogen atomic pairs move forward (backward) along the in-plane direction, leading to changes in the positive and negative charge centers, and thus, adjusting the electric dipole moment of the crystal. The two ferroelectric configurations can be transferred to each other by spatial rotation and connected through the centrosymmetric paraelectric structure. The value of the spontaneous polarization and depth of the double-well potential for monolayer SnS is found to be 262 pC/m and -40 meV. The corresponding values for single-layer SnSe are 151 pC/m and -3.76 meV. Such calculated parameters agree well with previous work [34,36]. The higher free-energy potential indicated that the paraelectric configuration is less stable than the ferroelectric phases, and
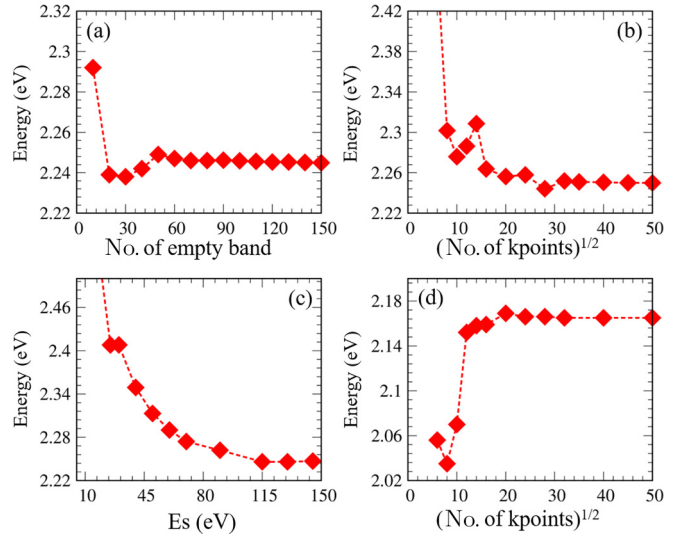
FIG. 6. Convergence of the G0W0 electronic band gap of SnS monolayer with respect to (a) number of empty bands, (b) k-grid, and (c) cutoff frequency. (d) the evolution of the first exciton states as functions of KPOINTS.

the former may transfer to the latter at a low temperature below the critical T_c. Under the ferroelectric-to-paraelectric-state transition, the symmetry of SnS and SnSe undergoes a transition from the asymmetry-to-symmetry characteristic. Such a transition is accompanied by the changing of electronic transport, the switching of BC dipole, and the appearance-to-disappearance transition of valley physics, Fig. 8. Specifically, owing to the crystal symmetry, the polarization of A and B excitons and their associated excitation energy could be affectively switched. From the experimental point of view, the switching between specific ferrovalley states has been achieved via the applied in-plane electric field [21].

The experimental confirmation of valley-selective linear dichroism in layered thin-film tin sulfide has been previously reported [26]. This study goes further to clarify the spontaneous valley-selective excitation in monolayer SnS and SnSe by using many-body first-principles calculations. In addition, we identified the underlying physical mechanisms that govern the interplay between valley physics, excitonic effects, and ferroelectricity. The exploration of light-matter interaction is of paramount importance as it indicates the potential for a practical experimental setup to generate the necessary exciton polarization for applications in valleytronics.

III. CONCLUSIONS

In summary, our study underscores the distinctive optical characteristics of single-layer orthorhombic SnS and SnSe, demonstrating their spontaneous linearly polarized optical selectivity, diverging from the valley-selective circular dichroism found in hexagonal lattices. 2D SnS and SnSe manifest the sizable electronic band gap, unique excitonic effects, and linear dichroism properties. By employing GW-BSE calculations and symmetry analysis, we reveal that the nonvanishing dipole moment for optical transitions between initial and final bands at specific valleys, as well as its associated exciton
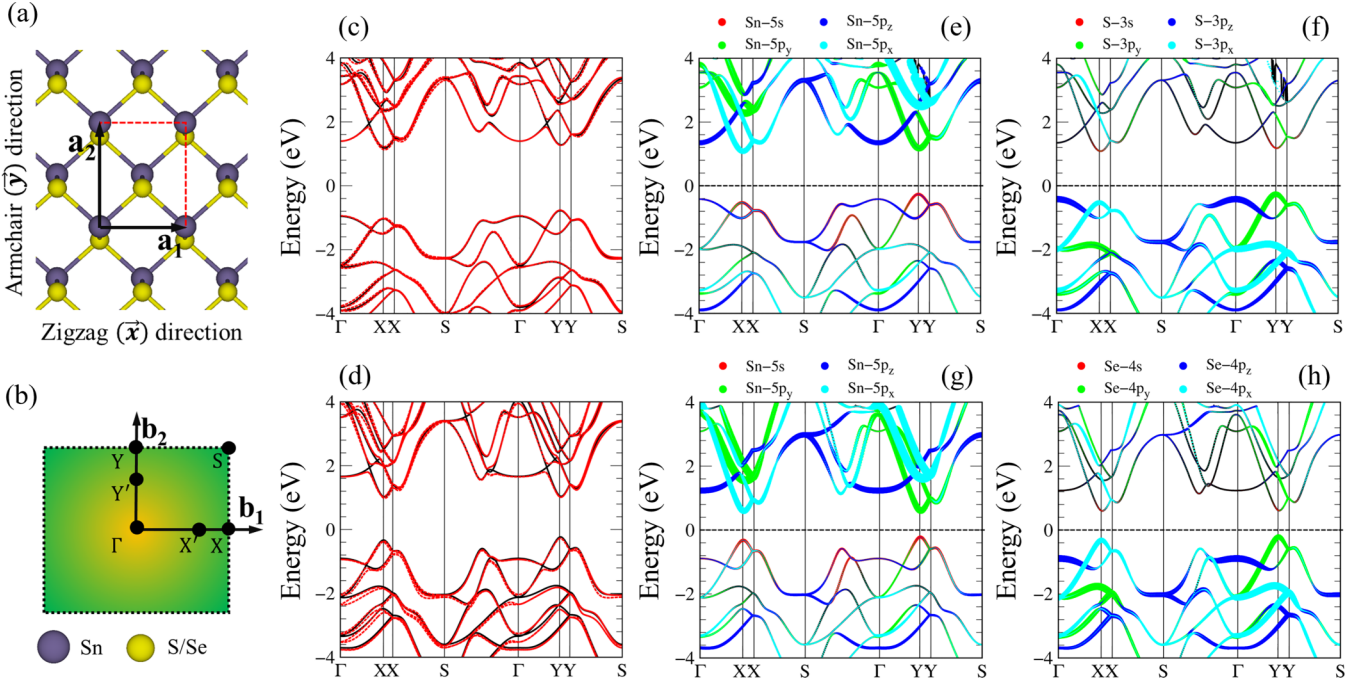
FIG. 7. The real (a) and the reciprocal space (b) of single-layer tin chalcogenides. Quasiparticle band structures of (c) SnS monolayer and (d) SnSe monolayer were calculated by using the G0W0 functionals. The black (red) color stands for the electronic band structure without (with) spin-orbit coupling. The orbital projected electronic band structure for (e) and (f) SnS monolayer, and (g) and (h) SnSe monolayer.

oscillation strength under particular polarization of incident light, is determined by the symmetry of these band pairs under mirror reflection. Furthermore, due to the in-plane distortion of tin and chalcogenide atoms, the layered SnS and SnSe exhibit a distinct ferroelectric property. Such ferroelectricity can interplay strongly with valley physics in monolayer SnS and SnSe, generating the coupled of these two scenarios in one monolayer system. Our exploration elucidates that manipulating incident light polarization and lattice distortion offers a robust means to control specific valley excitons in these materials, showcasing their potential for application in valleytronics.

ACKNOWLEDGMENTS

APPENDIX A: COMPUTATIONAL DETAILS

1. Ground state properties

We utilized the Vienna *Ab initio* Simulation Package (VASP) [57] with Perdew-Burke-Ernzerhof [58] generalized gradient approximation and projector-augmented wave pseudopotentials [59] for both ground state and excited state calculations. Our computations relied on a plane wave basis with a cutoff energy of 500 eV. For the monolayers of SnS and SnSe, we adopted a rectangular unit cell similar to the structure of phosphorene, while maintaining a 14 Å vacuum level to prevent interactions with periodic images.

2. GW-BSE calculations

To analyze quasielectronic band structures, we applied the single-shot GW (G0W0) method [60] to Kohn-Sham wave functions. 100 grid points for imaginary frequency and imaginary time points were used in this calculation. We conducted convergence tests employing diverse k meshes, varying cutoff energies for response functions, and adjusting the number of empty conduction bands. Our results (Fig. 6) demonstrated
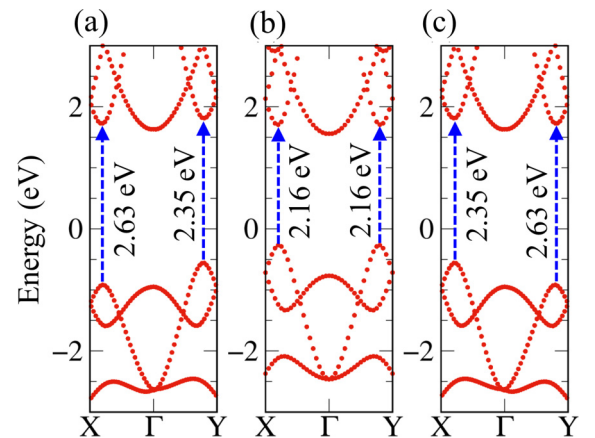
FIG. 8. Valley characteristics of the ferroelectric (a) P_y and (c) P_x phases, and (b) the paraelectric P_0 phase. Ferroelectricity breaks the fourfold rotational symmetry, making the valleys at X' and Y' no longer identical, which is the critical sign of spontaneous valley polarization. The global band gap of P_x and P_y exhibits the same characteristic, only the polarity of valley polarization is reversed. The valley splitting in the paraelectric phase, on the other hand, is absent due to its centrosymmetric structure.

TABLE II. Predicted mobility anisotropy of 2D tin chalcogenides.

	m_a/m_z (m$_0$)	E_a/E_z (eV)	C_a/C_z (Jm^{-2})	μ_a/μ_z (cm^{2}V^{-1}cm^{-1})
SnS(e)	0.19/0.22	3.52/2.80	42.15/20.95	2325.30/2680.49
SnS(h)	0.22/0.26	5.90/4.07	42.15/20.95	611.23/917.88
SnSe(e)	0.13/0.14	1.41/4.21	46.43/31.59	38167.22/3634.30
SnSe(h)	0.12/0.13	8.14/3.42	46.43/31.59	1347.48/6395.45

that employing a KPOINTS grid of $35\times35\times1$, a response function cutoff energy of 130 eV, and 100 empty conduction bands ensured convergence for the quasiparticle band gap.

To accurately determine the exciton spectrum, we investigated the convergence behavior of the BSE concerning parameters like the number of k points and involved electron-hole pairs. Our findings indicate a rapid convergence of the absorption spectra for the latter criterion. Specifically, considering only the four highest occupied valence bands and the three lowest unoccupied conduction bands adequately covers photon energies ranging from 0 to 4 eV. On the other hand, the BSE eigenvalues display notable sensitivity to the number of k-points utilized in the calculation. As depicted in Fig. 6(d), with an incremental increase in the k point, the energy levels of the excitonic states progressively ascend until reaching convergence, typically observed at around a 2000 k mesh.

APPENDIX B: SINGLE-PARTICLE TRANSITION DIPOLE MOMENTS

The probability of the optical transition [52] from the initial state $\varphi_{v\mathbf{k}}$ to the final state $\varphi_{c\mathbf{k}}$ is defined as $\langle\varphi_{v\mathbf{k}}|e^{i\mathbf{q}\cdot\mathbf{r}}\hat{e}\cdot\mathbf{p}|\varphi_{c\mathbf{k}}\rangle$, where $\mathbf{q}$ is the wave vector of the light interacting with the material, and $\hat{e}$ is the unit vector along the direction of optical polarization. Since the wavelength of light is usually much longer than the lattice constant of the semiconductor, one can assume $q \sim 0$ and $e^{i(\mathbf{q}\cdot\mathbf{r})} \sim 1$ in the dipole approximation [52,61].

By using the commutation relation $\mathbf{p} = \frac{im_0}{\hbar}[H, \mathbf{r}]$, the dipole moment $p_{vc\mathbf{k}}^{\mathbf{e}}$ of the transition between the states $\varphi_{v\mathbf{k}}$ and $\varphi_{c\mathbf{k}}$ is given by

$$p_{vc\mathbf{k}}^{\mathbf{e}} = \frac{im_0}{\hbar}\frac{1}{[\epsilon_{v\mathbf{k}} - \epsilon_{c\mathbf{k}}]}\langle\varphi_{v\mathbf{k}}|\mathbf{p}|\varphi_{c\mathbf{k}}\rangle. \quad (B1)$$

From Eq. (B1), we can calculate the dipole moment of the transition between two states with the given k-dependent Hamiltonian matrix.

APPENDIX C: ELECTRONIC TRANSPORT PROPERTIES

In order to establish a connection between the anisotropic band dispersion and electronic conductance, we utilized the deformation theory to estimate carrier mobility along the zigzag and armchair directions, as detailed in prior works

[29,42,62]. Given that monolayer tin chalcogenide exhibits in-plane anisotropy with distinct Cz and Ca parameters in the zigzag and armchair directions, respectively, the direction dependence of the charge carrier mobility is expected in SnS and SnSe monolayers. Particularly, the carrier mobility in the monolayer tin chalcogenide along the armchair (zigzag) direction can be estimated as follows [62]:

$$\mu_{i,a(z)}^{2D} \approx \frac{e\hbar^3\left(\frac{5C_{a(z)}+3C_{z(a)}}{8}\right)}{k_BTm_{i,a(z)}^*\sqrt{m_{i,a}^*m_{i,z}^*}\left(\frac{9E_{i,a(z)}^2+7E_{i,a(z)}+4E_{i,z(a)}^2}{20}\right)}. \quad (C1)$$

In this context, the index i indicates the type of the charge carrier. The symbol $m_{i,a(z)}^*$ represents the effective mass along the armchair (zigzag) direction. The elastic module $C_{a(z)}$ can be determined by fitting the quadratic relationship between the total energy E and the variation in lattice constant $\delta l/l_0$, expressed as $(C_{a(z)}/2)(\delta l/l_0)^2 = (E - E_0)/S_0$. Here, S_0 denotes the equilibrium lattice area of the 2D lattice. The deformation potential constant $E_{a(z)}^i = \partial E_{\text{edge}}/\partial\epsilon$ is obtained by examining the changes in the VBM or CBM due to slight lattice compression or expansion along the transport direction. The theoretical analysis is conducted at a room temperature of T = 300 K (Table II).

APPENDIX D: MODERN THEORY OF POLARIZATION

We used the modern theory of polarization [54] to calculate the spontaneous polarization, which is given by

$$P = \frac{e}{(2\pi)^3}Im\sum\int dk\langle\mu_{nk}|\nabla|\mu_{nk}\rangle + \frac{e}{\Omega}\sum Z^{ion}r, \quad (D1)$$

where Z^{ion} is the ionic charge plus the core electrons, r is the position of ions, Ω is the unit cell volume, e is the elementary charge, and μ_{nk} is the electronic wave function. The first term is the electronic contribution, and the second term is the contribution from ions and core electrons. The potential energy is then fitted using the Landau-Ginzburg expansion [34]:

$$E = \sum_i = \frac{A}{2}(P_i^2) + \frac{B}{4}(P_i^4) + \frac{C}{6}(P_i^6) + \frac{D}{2}\sum_{<i,j>}(P_i - P_j)^2. \quad (D2)$$

[1] A. K. Geim and K. S. Novoselov, Nat. Mater. **6**, 183 (2007).

[2] G. R. Bhimanapati, Z. Lin, V. Meunier, Y. Jung, J. Cha, S. Das, D. Xiao, Y. Son, M. S. Strano, V. R. Cooper *et al.*, ACS Nano **9**, 11509 (2015).

[3] T. Tan, X. Jiang, C. Wang, B. Yao, and H. Zhang, Advanced Science **7**, 2000058 (2020).

[4] K. S. Novoselov, A. Mishchenko, A. Carvalho, and A. H. Castro Neto, Science **353**, aac9439 (2016).

[5] J. R. Schaibley, H. Yu, G. Clark, P. Rivera, J. S. Ross, K. L. Seyler, W. Yao, and X. Xu, Nat. Rev. Mater. **1**, 16055 (2016).

[6] S. A. Vitale, D. Nezich, J. O. Varghese, P. Kim, N. Gedik, P. Jarillo-Herrero, D. Xiao, and M. Rothschild, Small **14**, 1801483 (2018).

[7] H. Zeng, J. Dai, W. Yao, D. Xiao, and X. Cui, Nat. Nanotechnol. **7**, 490 (2012).

[8] A. Rycerz, J. Tworzydło, and C. W. J. Beenakker, Nat. Phys. **3**, 172 (2007).

[9] W.-T. Hsu, Y.-L. Chen, C.-H. Chen, P.-S. Liu, T.-H. Hou, L.-J. Li, and W.-H. Chang, Nat. Commun. **6**, 8963 (2015).

[10] T. Cao, G. Wang, W. Han, H. Ye, C. Zhu, J. Shi, Q. Niu, P. Tan, E. Wang, B. Liu, and J. Feng, Nat. Commun. **3**, 887 (2012).

[11] P. Eickholt, C. Sanders, M. Dendzik, L. Bignardi, D. Lizzit, S. Lizzit, A. Bruix, P. Hofmann, and M. Donath, Phys. Rev. Lett. **121**, 136402 (2018).

[12] K. F. Mak, K. He, J. Shan, and T. F. Heinz, Nat. Nanotechnol. **7**, 494 (2012).

[13] S. Wu, J. S. Ross, G.-B. Liu, G. Aivazian, A. Jones, Z. Fei, W. Zhu, D. Xiao, W. Yao, D. Cobden, and X. Xu, Nat. Phys. **9**, 149 (2013).

[14] L. Li and F. Peeters, Appl. Phys. Lett. **114**, 243102 (2019).

[15] J. Lu, J. Yang, A. Carvalho, H. Liu, Y. Lu, and C. H. Sow, Acc. Chem. Res. **49**, 1806 (2016).

[16] R. Guo, X. Wang, Y. Kuang, and B. Huang, Phys. Rev. B **92**, 115202 (2015).

[17] L. Cheng, D. Li, X. Dong, Q. Ma, W. Yu, X. Wang, H. Yu, J. Wang, and G. Liu, Mater. Res. **20**, 1748 (2017).

[18] S. Guo, L. Yuan, X. Liu, W. Zhou, X. Song, and S. Zhang, Chem. Phys. Lett. **686**, 83 (2017).

[19] A. S. Pawbake, S. R. Jadkar, and D. J. Late, Mater. Res. Express **3**, 105038 (2016).

[20] W. Yang, C. Zhao, B. Du, R. Wu, X. Lai, Y. He, and J. Jian, Sens. Actuat. B **370**, 132407 (2022).

[21] N. Higashitarumizu, H. Kawamoto, C.-J. Lee, B.-H. Lin, F.-H. Chu, I. Yonemori, T. Nishimura, K. Wakabayashi, W.-H. Chang, and K. Nagashio, Nat. Commun. **11**, 2428 (2020).

[22] Y. Bao, P. Song, Y. Liu, Z. Chen, M. Zhu, I. Abdelwahab, J. Su, W. Fu, X. Chi, W. Yu *et al.*, Nano Lett. **19**, 5109 (2019).

[23] A. S. Rodin, L. C. Gomes, A. Carvalho, and A. H. Castro Neto, Phys. Rev. B **93**, 045431 (2016).

[24] Z. Tian, C. Guo, M. Zhao, R. Li, and J. Xue, ACS Nano **11**, 2219 (2017).

[25] J. Xia, X.-Z. Li, X. Huang, N. Mao, D.-D. Zhu, L. Wang, H. Xu, and X.-M. Meng, Nanoscale **8**, 2063 (2016).

[26] C. Chen, X. Chen, Y. Shao, B. Deng, Q. Guo, C. Ma, and F. Xia, ACS Photon. **5**, 3814 (2018).

[27] K. F. Mak, D. Xiao, and J. Shan, Nat. Photonics **12**, 451 (2018).

[28] A. A. Mostofi, J. R. Yates, Y.-S. Lee, I. Souza, D. Vanderbilt, and N. Marzari, Comput. Phys. Commun. **178**, 685 (2008).

[29] J. Qiao, X. Kong, Z.-X. Hu, F. Yang, and W. Ji, Nat. Commun. **5**, 4475 (2014).

[30] L. C. Gomes and A. Carvalho, Phys. Rev. B **92**, 085406 (2015).

[31] J. R. Brent, D. J. Lewis, T. Lorenz, E. A. Lewis, N. Savjani, S. J. Haigh, G. Seifert, B. Derby, and P. O'Brien, J. Am. Chem. Soc. **137**, 12689 (2015).

[32] P. Z. Hanakata, A. Carvalho, D. K. Campbell, and H. S. Park, Phys. Rev. B **94**, 035304 (2016).

[33] R. Fei, W. Li, J. Li, and L. Yang, Appl. Phys. Lett. **107**, 173104 (2015).

[34] R. Fei, W. Kang, and L. Yang, Phys. Rev. Lett. **117**, 097601 (2016).

[35] K. Chang, F. Kuster, B. J. Miller, J.-R. Ji, J.-L. Zhang, P. Sessi, S. Barraza-Lopez, and S. S. Parkin, Nano Lett. **20**, 6590 (2020).

[36] A. Priydarshi, Y. S. Chauhan, S. Bhowmick, and A. Agarwal, J. Appl. Phys. **131**, 034101 (2022).

[37] J. Kim, K.-W. Kim, D. Shin, S.-H. Lee, J. Sinova, N. Park, and H. Jin, Nat. Commun. **10**, 3965 (2019).

[38] L. Xu, M. Yang, S. J. Wang, and Y. P. Feng, Phys. Rev. B **95**, 235434 (2017).

[39] G. Shi and E. Kioupakis, Nano Lett. **15**, 6926 (2015).

[40] V. K. Dien, P. T. B. Thao, N. T. Han, N. D. Khanh, L. V. P. Thuan, M. F. Lin, and N. T. Tien, Phys. Rev. B **108**, 205406 (2023).

[41] S. H. Mir, V. K. Yadav, and J. K. Singh, ACS Omega **5**, 14203 (2020).

[42] R. Fei and L. Yang, Nano Lett. **14**, 2884 (2014).

[43] A. Srivastava, M. Sidler, A. V. Allain, D. S. Lembke, A. Kis, and A. Imamoğlu, Nat. Phys. **11**, 141 (2015).

[44] J. Qi, X. Li, Q. Niu, and J. Feng, Phys. Rev. B **92**, 121403(R) (2015).

[45] X. Leng, F. Jin, M. Wei, and Y. Ma, Wiley Interdiscip. Rev.: Comput. Mol. Sci. **6**, 532 (2016).

[46] D. Y. Qiu, F. H. da Jornada, and S. G. Louie, Phys. Rev. Lett. **111**, 216805 (2013).

[47] K. He, N. Kumar, L. Zhao, Z. Wang, K. F. Mak, H. Zhao, and J. Shan, Phys. Rev. Lett. **113**, 026803 (2014).

[48] M. L. Trolle, T. G. Pedersen, and V. Véniard, Sci. Rep. **7**, 39844 (2017).

[49] D. Y. Qiu, F. H. da Jornada, and S. G. Louie, Phys. Rev. B **93**, 235435 (2016).

[50] G. Antonius, D. Y. Qiu, and S. G. Louie, Nano Lett. **18**, 1925 (2018).

[51] C. Vorwerk, C. Cocchi, and C. Draxl, Phys. Rev. B **95**, 155121 (2017).

[52] M. Fox, *Optical Properties of Solids* (Oxford University Press, Oxford, 2010).

[53] Y. Yao, L. Kleinman, A. H. MacDonald, J. Sinova, T. Jungwirth, D.-S. Wang, E. Wang, and Q. Niu, Phys. Rev. Lett. **92**, 037204 (2004).

[54] R. Resta, Rev. Mod. Phys. **66**, 899 (1994).

[55] H. Wang, X. Tang, H. Xu, J. Li, and X. Qian, npj Quantum Mater. **7**, 61 (2022).

[56] Y. Xu, Y. Wang, S. Wang, S. Yu, B. Huang, Y. Dai, and W. Wei, Nano Lett. **22**, 9147 (2022).

[57] J. Hafner, J. Comput. Chem. **29**, 2044 (2008).

[58] B. Hammer, L. B. Hansen, and J. K. Nørskov, Phys. Rev. B **59**, 7413 (1999).

[59] G. Kresse and D. Joubert, Phys. Rev. B **59**, 1758 (1999).

[60] M. Shishkin and G. Kresse, Phys. Rev. B **75**, 235102 (2007).

[61] V. Wang, N. Xu, J.-C. Liu, G. Tang, and W.-T. Geng, Comput. Phys. Commun. **267**, 108033 (2021).

[62] H. Lang, S. Zhang, and Z. Liu, Phys. Rev. B **94**, 235306 (2016).